# 3D printed multifunctional PEEK bone scaffold for multimodal treatment of osteosarcoma and osteomyelitis

Ce Zhu[1,2#], Miaomiao He[1#], Dan Sun[3], Yong Huang[1], Leizhen Huang[1], Meixuan Du[1], Jingcheng Wang[1], Juehan Wang[1], Zhongyang Li[1], Limin Liu[1], Yueming Song, Yubao Li[1], Ganjun Feng[1]*, Li Zhang[1]*

1. Department of Orthopedic Surgery and Orthopedic Research Institute, West China Hospital, Analytical & Testing Center, Sichuan University, Chengdu 610065, China

2. Department of Spine Surgery, The Affiliated Hospital of Southwest Medical University, Luzhou, China.

3. Advanced Composite Research Group, School of Mechanical and Aerospace Engineering, Queen's University Belfast, Belfast, BT9 5AH, UK

* Corresponding authors

E-mail address: gjfenghx@163.com (Ganjun Feng); nic1976@scu.edu.cn (Li Zhang)

**Abstract**: In this work, we developed the first 3D PEEK based bone scaffold with multi-functions targeting challenging bone diseases such as osteosarcoma and osteomyelitis. 3D printed PEEK/graphene nanocomposite scaffold was deposited with drug laden (antibiotics and/or anti-cancer drugs) hydroxyapatite coating. The graphene nanosheets within the scaffold served as effective photothermal agents that endowed the scaffold with on-demand photothermal conversion function under NIR laser irradiation. The bioactive hydroxyapatite coating significantly boosted the stem cell proliferation *in vitro* and promoted the new bone growth *in vivo*. The presence of antibiotics and anti-cancer drugs enabled eradication of drug resistant bacteria as well as ablation of osteosarcoma cancer cells, the treatment efficacy of which can be further enhanced by the on-demand laser induced heating. The promising results demonstrate the strong potential of our multi-functional scaffold in applications such as bone defect repair as well as multimodal treatment of osteosarcoma and osteomyelitis.

## Introduction

Osteosarcoma (OS) is the most common type of primary bone cancer and it usually occurs in children and adolescents aged 10-19 years [1]. It is mostly found in the long bones of the lower extremity and metastasis is diagnosed in 20% of patients [2]. Osteomyelitis (OM) on the other hand, is a bacterial induced bone infection which also targets a considerable number of patients, particularly children, elderly, and patients with comorbidities (e.g. diabetics). The disease can lead to serious functional impairment, long-lasting disability, permanent handicap and even life threatening conditions. Both bone diseases are challenging clinical conditions, and the treatment protocol usually involves resection of the diseased bone tissue, followed by use of anti-cancer or antibiotic drugs. The treatment would inevitably result in large bone defect beyond the bone's self-healing ability (critical size bone defect), and the patients often suffer from recurrence of the diseases due to the residual cancer cell or bacteria.

Multimodal therapy, such as chemo-photothermal therapy (chemo-PTT) [3], photothermal/photodynamic therapy (PTT/PDT) [4], PDT/chemotherapy therapy [5] etc, are emerging strategies for the treatment of osteosarcoma and osteomyelitis. For instance, in chemo-PTT of bone cancer, cancer drugs can be delivered to the tumorous tissue in the targeted area, and the near-infrared (NIR) laser induced heating can enhance the sensitivity of tumor cells towards chemotherapy, leading to reduced drug dosage and improved treatment efficacy [6]. Combined use of laser heating and antibiotics is also known to enhance bacterial eradication at the infection site [7], which can be potentially used for osteomyelitis treatment.

To date, chemo-PTT is mainly achieved through local delivery of nanomaterials such as $CuFeSe_2$ [8], $Fe-CaSiO_3$ [9], graphene oxide [10], etc, which act as drug delivery vehicles and photothermal (PT) conversion agents. Some researchers also

attempted to introduce PT conversion agents and drugs into hydrogels (such as pNIPAAm-co-pAAm) [11] or 3D porous ceramic (such as β-TCP) [10] or polymer (such as chitosan) scaffolds [12] for bone repair and chemo-PTT therapy. However, the above mentioned materials cannot provide sufficient mechanical properties, which would impede their applications, particularly in load-bearing bone repair [13, 14].

In the past decade, polyetheretherketone (PEEK) has attracted increased attention in the biomedical field. PEEK has outstanding properties such as biocompatibility [15], X-ray/thermal/chemical stability [16], and mechanical properties (elastic modulus) similar to that of the human bone [7]. Being a FDA approved biomaterial, PEEK has been successfully deployed in applications such as artificial knee joints [17], spine fusion [18], skull [19], and orthopedic implants [20], etc. Its thermoplastic nature also allows it to be 3D printed into tissue scaffold with be-spoke geometry [21]. One major limitation of PEEK is its lack of bioactivity, which impedes its application for bone regeneration [22, 23]. To address this issue, various strategies (such as surface coating or bulk reinforcement with bioactive agents) have been adopted to enhance the bioactivity of PEEK implants, a detailed review of which can be found in [24].

In the present study, we created a highly functional 3D printed PEEK/graphene composite scaffold with drug laden bioactive coating. The graphene nanosheets within the scaffold act as strong photothermal conversion agent, while the loaded drugs (such as antibiotics stearyltrimethylammonium chloride (STAC), and/or cancer drug cisplatin (DDP)) enabled effective cancer and/or bacteria eradication with the aid of NIR laser induced heating. The scaffold has been sucessfully demonstrated for bone regeneration, as well as multimodal treatment (chemo-PTT) of cancer ablation and bacterial eradication. We believe our multi-functional bone scaffold can potentially serve as a new platform for the management of challenging bone diseases such as osteosarcoma and osteomyelisis.
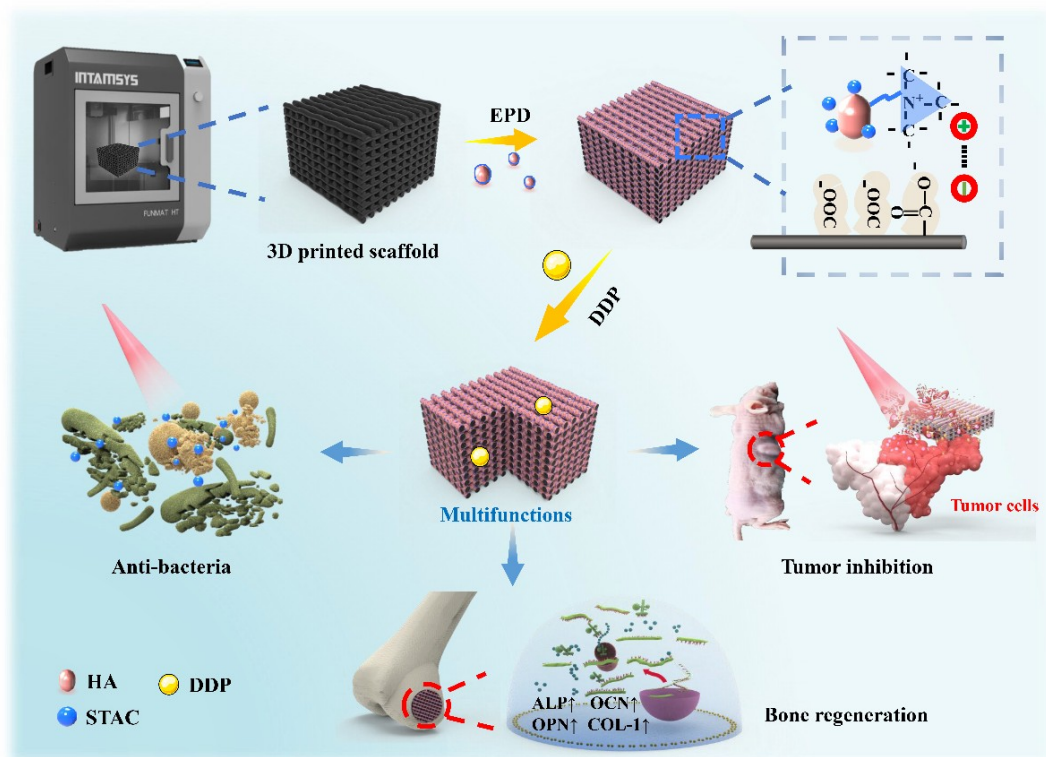
**Scheme 1**. Schematic showing scaffold preparation and its associated multi-functions

## Materials and Methods

### Preparation of 3D printed PEEK scaffold

PEEK powder (particle size ~ 500 µm, Jilin Joinature Polymer Co., Ltd., China) was dried in an 80 ℃ oven for 12 h before use. Graphene (G) nanosheets (~ 5 layers, maximum radial size 2~4 µm, average aspect ratio ~ 4500) were supplied by the Sixth Element (Changzhou) Materials Technology Co., Ltd. China. PEEK powder with 10 wt% G were dispersed in ethanol and sonicated at 25 ℃ for 30 min. After filtration and drying, the power mixture was spun into filaments for further 3D printing (Funmat HT, Intamsys, Shanghai, China) of PEEK/G composite (PG) scaffold. 3D printed scaffolds (100 mm × 100 mm × 4 mm) with simple cubic lattice structure and different pore size (200 µm and 500 µm, respectively) were prepared. The PG scaffold were then plasma treated to modify the surface with oxygen rich functional groups, which can facilitate the subsequent electrophoretic deposition process. 3D printed pristine PEEK (P) scaffold was also prepared for comparison.

4

**Preparation of HA coated PG scaffold**

Hydroxyapatite (HA) was synthesized by hydrothermal method according to established procedures [25, 26]. Positively charged stearyltrimethylammonium chloride (STAC) (Aladdin, China) was loaded onto HA particles through physisorption and uniformly dispersed STAC/HA suspension was used for subsequent electrophoretic coating deposition.

Electrophoretic deposited STAC/HA coating was deposited onto the 3D PEEK scaffold following [7] under a DC voltage of 50 V for 60 min with a carbon rod being the anode and PG scaffold being the cathode. The coated scaffold was named as PGH. The coated scaffold was then immersed in sodium chloride solution of cisplatin (DDP, 1 mg/mL) following [27] for anti-cancer drug loading, and the final drug laden scaffold is named as PGHD .

**Characterization**

*Materials characterization*

Mechanical testing coupons (10 mm × 10 mm × 4 mm) and electrical conductivity testing coupons (100 mm × 100 mm × 1 mm) were produced from hot pressed P and PG sheet. Compressive tests were performed using universal mechanical testing machine (MTS, model E45, USA) at a speed of 1 mm/min, following GB/T 1041-2008/ISO 604:2002. Four-point probes method (RTS-8, Tianjin Nuleixinda Technology Co., Ltd., China) was used for electrical conductivity measurements. X-ray photoelectron spectroscopy analysis (XPS, XSAM800, Kratos, England) was performed to confirm the elemental state of PG before and after plasma treatment. Zeta potential (Zetasizer Nano ZS, Malvern, England) was used to determine the surface charge of the STAC-HA particles. Scanning electron microscope (SEM, JSM-7500F, JEOL, Japan) and EDS (JSM-7500F, JEOL, Japan) were used to analyze the morphology and elemental information of HA and the coating deposited on PGH.

The photothermal conversion effect of all samples was analyzed in air and in

phosphate buffered solution (PBS), respectively. A 808 nm NIR laser (0-2 $W/cm^2$, Richeng Science and Technology Development Co. LTD, Shanxi, China) was used at different laser power densities (0.05 $W/cm^2$, 0.15 $W/cm^2$, 0.30 $W/cm^2$) and the temperature of the scaffold was monitored in real time using an infrared thermal imaging system (TiS20+, Fluke, USA). The temperature data were analyzed using FLUKE software.

For drug release analysis, PGHD (10 mm ×10 mm × 4 mm) was immersed in 5 ml deionized water and placed in a shaking incubator under 37 ℃. The cumulative release of DDP (Pt element) was detected by Inductively Coupled Plasma Emission Spectroscopy (ICP-OES, AXIS Ultra DLD, Kratos, UK) at different time intervals (1 h, 3 h, 10 h and 24 h). XPS was performed to detect the state of Pt element.

*Antibacterial testing*

Gram-negative *Escherichia coli* (*E. coli*, ATCC25922) and gram-positive *Methicillin-resistant Staphylococcus aureus* (MR*SA*, ATCC29213) were used to evaluate the antibacterial properties of the P, PG, PGH and PGHD scaffolds. Ten-fold dilution method was used to quantitatively measure the bactericidal rate (BR) defined by **Eq.1** [28]. Briefly, bacterial strain was incubated in culture medium for 24 h and the subculture from the second passage was used as the pre-made bacterial fluid. 50 µL pre-made bacterial fluid was drop-casted onto scaffold samples and incubated for 2 h followed by topping of 4 mL physiological saline. The mixture of bacterial fluid and physiological saline extracted from each sample was subsequently diluted $10^4$ times. Finally, 50 µL of each diluted fluid sample was inoculated on nutrient Luria-Bertani agar plate. The number of bacterial colonies up to 30~300 CFU (colony-forming unit) was counted.

$$BR(\%) = \frac{n_0 - n}{n_0} \times 100 \%$$ **Eq.1**

Where $n_0$ is the number of colonies in the control group, $n$ is the number of colonies in the experimental group.

To investigate the effect of photothermal conversion on bacteria eradication, a separate set of scaffold samples were irradiated by NIR laser for 10 min before the ten-fold dilution method was applied. The bacterial fluid irradiated by NIR laser was used as the control (named NIR only).

*Tumor ablation experiments*

MG-63 cells were seeded in a 48-well plate at a density of $1.0 \times 10^4$ cells/well using DMEM with high glucose (Hyclone) supplemented with 10% fetal bovine serum (FBS, Gibco). The seeded cells were kept in an incubator containing 5% $CO_2$ at 37 ℃. The scaffolds were gently placed into the plate after the incubation for 24 h. Subsequently, the scaffolds were irradiated by an 808-nm NIR laser at 0.30 $W/cm^2$ for 5 min. Cultured scaffold with no NIR irradiation was used as the control. After a 12h incubation post NIR irradiation, cell viability was measured by Cell Counting Kit-8 (CCK8, Beijing Solarbio Science and Technology, China) assay.

In order to quantify the photothermal effect on ablation of tumor cells, the cell viability on scaffolds was observed by staining live cells with Calcein AM and dead cells with Propidium iodide (Live/Dead Kit, Beijing Solarbio Science and Technology, China) 12 h after the irradiation (0.30 $W/cm^2$, 5 min). Images of live (green) and dead (red) cells were scanned under inverted fluorescence microscope (Olympus IX83).

Confocal laser scanning microscopy (CLSM, Nikon) was used to observe the cytoskeleton of cells on different scaffolds with or without NIR irradiation. Cells ($10^4$ cells/well) were seeded on P, PG, PGH, and PGHD scaffolds respectively and cultured for 24 h in 48-well plates. The samples were then irradiated by NIR laser (0.30 $W/cm^2$) for 5 min, with non-irradiated cells being the control group. After 12 h, the cytoskeleton and cell nuclei were stained with Phalloidin-iFluor™ 555 Conjugate (AAT Bioquest, USA) and DAPI (Beijing Solarbio Science and Technology, China), respectively.

Male BALB/c nude mice were subcutaneously injected with UMR-106-LUC cells ($4\times10^6$ cells) to establish the ectopic osteosarcoma models [10]. When the

diameter of tumor reached 6~8 mm, the mice were randomly divided into ten groups (n = 4 in each group), namely: Control; Control+ NIR; P; P+ NIR; PG; PG+ NIR; PGH; PGH+ NIR; PGHD; PGHD+ NIR. A skin incision was made on the edge of the tumor, and different scaffolds (5 mm×1 mm ×1 mm) were inserted into the center of the tumor. Mice in the NIR groups were irradiated by NIR (0.30 W/cm$^2$) for 10 min daily and the temperature of the tumor tissue was monitored by an infrared thermal imaging system (TiS20+, FLUKE, USA). The temperature data were analyzed using FLUKE software. Day 0 denotes the date of the first laser treatment. The tumor sizes were measured every two days using a vernier caliper. The tumor volume ($V_t$) was calculated following:

$$V_t = L \times W^2/2 - V_s \hspace{4cm} \textbf{Eq.2}$$

Where L is the tumor length, W is the tumor width, $V_s$ is the scaffold volume (5 mm$^3$). Relative tumor volume is defined as

$$V_{rt} = V_t/V_{t0} \hspace{4cm} \textbf{Eq.3}$$

Where $V_{t0} = V_t$ (day 0) $- V_s$.

The body weight of the mice was also recorded every two days. Whole-body fluorescent imaging was performed on day 0 and day 10, respectively. On day 11, the mice were sacrificed and the tumors were harvested along with the heart, liver, spleen, lungs and kidney to evaluate the potential side effect of the scaffolds and/or the laser treatment. The tissue and organs were infiltrated with 4% paraformaldehyde, embedded in paraffin, and finally stained with hematoxylin and eosin (H&E).

*Cytocompatibility and Bone Regeneration*

Mouse MC3T3-E1 pre-osteoblasts (10$^4$ cells/well) were seeded in 48-well culture plates containing different scaffolds with α -MEM (Hyclone) supplemented with 10% FBS (Gibco) and 1% Penicillin-Streptomycin-L-glutamine (Hyclone) in a humidified incubator containing 5% $CO_2$ at 37 ℃. 24 h after incubation, the seeded scaffolds were rinsed with PBS three times and fixed by 4% paraformaldehyde solution for 15 min. The morphology and adhesion of MC3T3-E1 cells on the scaffolds was observed by confocal laser scanning microscopy (CLSM, Nikon). The

cytoskeleton and cell nuclei were stained with Phalloidin-iFluor™ 555 Conjugate (AAT Bioquest, USA) and DAPI (Beijing Solarbio Science and Technology, China), respectively.

To investigate the proliferation of cells on the scaffolds, $10^4$ MC3T3-E1 cells were seeded in 48-well plates containing scaffolds at 37 ℃ with 5% $CO_2$. The cell proliferation on different scaffolds was assessed on day 1, 3, 5, and 7 by cell counting kit (CCK-8; Dojindo, Japan). Briefly, the culture medium was removed and 10% CCK-8-containing medium was added to each well in dark. After 2 h of incubation, 100 μL CCK-8 solution was transferred to a 96-well plate and examined by Multiscan Spectrum (Synergy Mx, Biotek, USA) at 450 nm. To study the scaffolds biocompatibility, MC3T3-E1 cells (1.0 ×$10^4$ cells/well) were seeded in a 48-well plate and the scaffolds were gently placed into the plate 24 h later. After an additional 24 h of incubation, the scaffolds were removed and the cells in the plate were stained with PI and Calcein-AM, respectively. Finally, cells were observed under a fluorescence microscope (Olympus IX83).

Mouse MC3T3-E1 pre-osteoblasts were seeded in 48-well plate at a density of $10^4$ cells/well with α -MEM (Hyclone) supplemented with 10% FBS (Gibco) and 1% Penicillin-Streptomycin-L-glutamine (Hyclone). 48 h after incubation, the cells reached confluence and the growth medium was removed and replaced with osteogenic medium comprising growth media supplemented with dexamethasone (100 nM; Sigma), L-ascorbic acid (50 μg/mL; Sigma), and β-glycerophosphate (10 mM; Sigma). The scaffolds were gently placed into the plate and the medium was replaced every 2 days.

The expressions of osteogenesis-related genes were quantitatively analyzed by real-time reverse-transcriptase polymerase chain reaction (real-time PCR) on day 7. The total RNA was extracted using Trizol reagent (Invitrogen, USA) and the complementary DNA (cDNA) was obtained by synthesizing DNA from 1 μg of total RNA via reverse-transcription using an iScript cDNA Synthesis Kit (Bio-Rad) following the manufacturer's instructions. Real-time PCR was performed with

EvaGreen Dye (Bio-Rad) using RT-PCR instrument (CFX Connect, Bio-Rad). The forward and reverse primers for different genes were listed in **Table S1**. Cycle threshold (Ct) values were used to determine fold differences according to the $\Delta\Delta$Ct method. β-actin was used as an internal reference to normalize the data.

On day 10, two representative osteogenic proteins (OPN and OCN) were evaluated by immunofluorescence. The cells co-cultured with different scaffolds were fixed in 4% paraformaldehyde for 10 min, permeabilized with 0.25% Triton X-100 for 5 min, and incubated with 1% bovine serum albumin (BSA) for 1h at room temperature. Then the cells were incubated with primary antibodies in 1% BSA overnight at 4 ℃ (mouse anti-OPN monoclonal antibody, 1:50, Novus; rabbit anti-OCN polyclonal antibody, 1:100, Absin). The cells were then incubated in dark with 1:500 dilution of secondary antibodies in 1% BSA for 1h at room temperature (Alexa Fluor® 488-conjugated anti-mouse IgG and Alexa Fluor® 555-conjugated anti-rabbit IgG, Cell Signaling). Finally, the cytoskeleton and nuclei were stained with phalloidin (Phalloidin-iFluor™ 555 Conjugate, AAT Bioquest; AbFluor™ 488-Phalloidin, Abbkin) and DAPI (Beijing Solarbio Science and Technology, China), respectively. All staining were followed by rinsing with PBS three times. Representative images were obtained using a fluorescence microscope (Olympus IX83).

Alkaline phosphate (ALP) activity of MC3T3-E1 pre-osteoblasts with different scaffolds was quantified using ALP activity assay kit (Beijing Solarbio Science and Technology, China) on day 7. Briefly, cells were removed from the scaffold surfaces using Triton X-100 (1% v/v) and then centrifuged (12,000 rpm at 4 ℃) for 30 min to remove all cell debris. The supernatant was mixed with p-nitrophenyl phosphate (Songon) at 37 ℃ for 60 min. 4-Nitrophend NaOH was added to the cell supernatant and the ALP activity was examined by Multiscan Spectrum (Synergy Mx, Biotek, USA) at 510 nm. For standardization, the total protein content was calculated by a bicinchoninic acid (BCA) protein assay kit (Beyotime). The ALP activity was ultimately expressed as the total protein content (μM/mg). For ALP staining, the cells were fixed with 4% paraformaldehyde for 15 min, followed by staining using azo-

coupling ALP color development kit (Beijing Solarbio Science and Technology, China) for 20 min in dark. Finally, cells were imaged using a fluorescence microscope (Olympus IX83).

The calcium nodules formed by the MC3T3-E1 cells co-cultured with different scaffolds were stained by Alizarin Red S (Al, Sigma, USA) on day 21. Specifically, cells were fixed in 4% paraformaldehyde for 15 min. The cells were washed thrice with distilled water and stained with Al for 20 min. Afterwards, the excess Al was thoroughly removed with distilled water and the deposited calcium was imaged. For quantitative analysis, the stained samples were dissolved with 10% cetylpyridinium chloride and analyzed by a Multiscan Spectrum (Synergy Mx, Biotek, USA) at 600 nm.

*Bone regeneration in vivo*

All surgical procedures were approved by the Animal Ethics Committee of West China Hospital of Sichuan University, China. Sixteen male Sprague-Dawley (SD) rats (8 weeks old, 200 ± 20 g) were chosen to construct distal femoral condyle defect models for the evaluation of bone osseointegration *in vivo*. The rats were randomly split into four groups: P, PG, PGH and PGHD, and were anaesthetized by isoflurane. A hole (3 mm in diameter and 7 mm in depth) was made using a dental drill and the scaffold sample was press fit into the hole. 8 weeks post-surgery, the rats were sacrificed and their femurs were used for micro-CT scanning and histological staining.

Polychrome sequential fluorescent labeling was used to characterize the new bone formation and mineralization. 30 mg/kg alizarin red S (Al, Sigma, USA) and 20 mg/kg calcein (CA, Sigma, USA) were administered intraperitoneally 3 and 6 weeks post-surgery, respectively.

Micro-CT (Quantum GX, Perkin Elmer, USA) scanning was carried out at 80 kV and a resolution of 25 μm 4 and 8 weeks post-surgery, respectively. New bone formation was analyzed quantitatively based on bone volume/tissue volume (BV/TV), trabecular number (Tb. N), and trabecular separation (Tb. Sp).

The harvested femoral specimen were fixed by 4% buffered paraformaldehyde, dehydrated using graded ethanol solution (70%, 85%, 95% and 100%), and embedded in polymethylmethacrylate without decalcification. The specimens were then microtomed into 5 μm thick slices along the cross-sectional surface, stained by methyl blue and basic fuchsin and observed under optical microscopy (Olympus IX83). The area of new bone tissue was calculated by the Image J software. Fluorescence observation was performed using CLSM (Nikon, Japan). The excitation/emission wavelengths used to observe the chelating fluorochromes were 543/620 nm and 488/520 nm for alizarin red S (AL, red) and calcein (CA, green), respectively.

*Statistical analysis*

Statistical analysis was performed using SPSS software (version 22.0; IBM Corp., Armonk, NY, USA), and the statistical significance was analyzed using one-way analysis of variance (ANOVA) followed by the LSD *post hoc test*. The relationships between different parameters were performed using Pearson's correlation test. Statistical significance was considered for *p < 0.05*, while high significance was *p < 0.01*.

## Results and discussion

**Fig 1a** show the compressive moduli data of P and PG scaffolds with different pore size. Both mechanical properties decrease with increasing scaffold pore size. The scaffolds with 500 μm pores demonstrated compressive moduli comparable to that of human cancellous bone (<3 GPa) [29], and are therefore selected for further investigation. The electrical conductivity of PG is $2.75 \times 10^{-3}$ S/cm (**Fig 1b**), which is twelve order of magnitude higher than that of pristine P (~$10^{-15}$ S/cm), and is comparable to semiconducting material. **Fig 1c** shows the XPS spectra of PG before plasma. Deconvolution of C1s shows that 284.6 eV can be attributed to C-C/C-H bond, 286.2 eV and 288.3 eV can be assigned to C-O bond and C=O bond, respectively. The bond at 291.4 eV has been ascribed to π-π* conjugation between G

and PEEK. It is worth noting that the presence of such π-π* conjugation could have provided the potential electron migration pathway, which contribute to the greatly enhanced electrical conductivity of PG. The deconvolution of O1s (**Fig 1d**) shows that the characteristic peaks at 531.8 eV is attributed to O=C and 533.2 eV to O-C. After activated by plasma treatment, oxygen containing groups shows are located at 533.5 eV (-COOH), 532.8 eV (C-O-C/-C-OH) and 531.8 eV (C=O), respectively, see **Fig 1e**. Before the coating deposition, the surface charge of STAC loaded HA nanoparticles (STAC/HA) was analyzed to select the optimal drug loading ratios. **Fig 1f** shows the Zeta potential of STAC loaded HA nanoparticles (STAC/HA) with different drug loading ratios (0:10, 3:10 and 5:10). STAC/HA with drug loading ratio 3:10 exhibits a strong positive Zeta potential (>30 mV) and excellent dispersion (Faraday-Tyndall effect) (**Fig 1f** inset), and hence was chosen for the subsequent coating deposition.
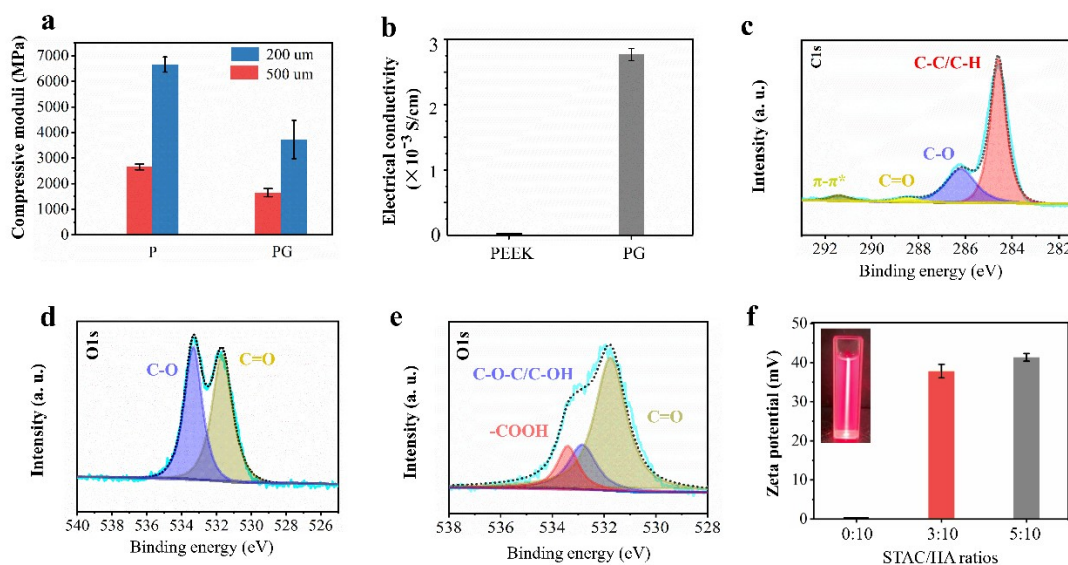


**Fig 1**. (**a**) The compressive moduli of pristine PEEK and PG composite scaffold with different pore size; (**b**) the electrical conductivity of PEEK and PG composite; (**c**) C1s deconvolution of P/G before plasma treatment; O1s deconvolution of P/G before (**d**) and after (**e**) plasma treatment; (**f**) Zeta potential of STAC loaded HA nanoparticles;

Fig 2a shows that the SEM images of the 3D printed PG scaffold before and after coating deposition, as well as a closeup image of the coating morphology. EDS mapping for elements Ca and P (see **Fig 2b**) further confirms that EPD has been

sucessfully deployed to deposit coatings onto both the scaffold exterior and interior. The results can be further corroborated by the Zeta potential of the scaffold surface before and after EPD deposition of STAC/HA, which changed from -40.73 ± 1.25 mV to 14.90 ± 4.91 mV (**Fig 3a**). The drastic variation in its surface charge suggest the successful grafting of STAC/HA coating *via* electrostatic interaction.
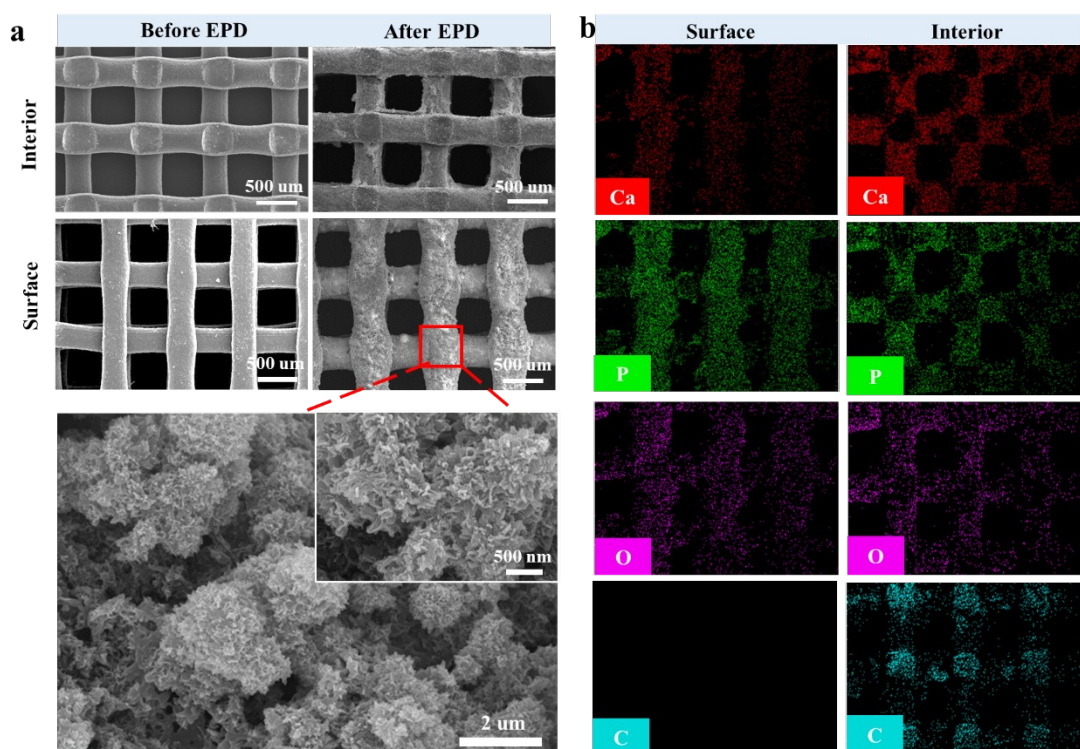


**Fig 2**. (**a**) the surface and interior SEM images of PG before and after EPD compared with HA particles; (**b**) the surface and interior EDS of PG after EPD.

The SEM image of PGHD and the associated EDS mapping shown in **Fig 3b** confirms that after loading of DDP, the drug has been evenly distributed on the scaffold surface. XPS analysis on Pt 4f deconvolution (**Fig 3c**) further confirmed the chemical state of Pt, indicating the successful loading of DDP.
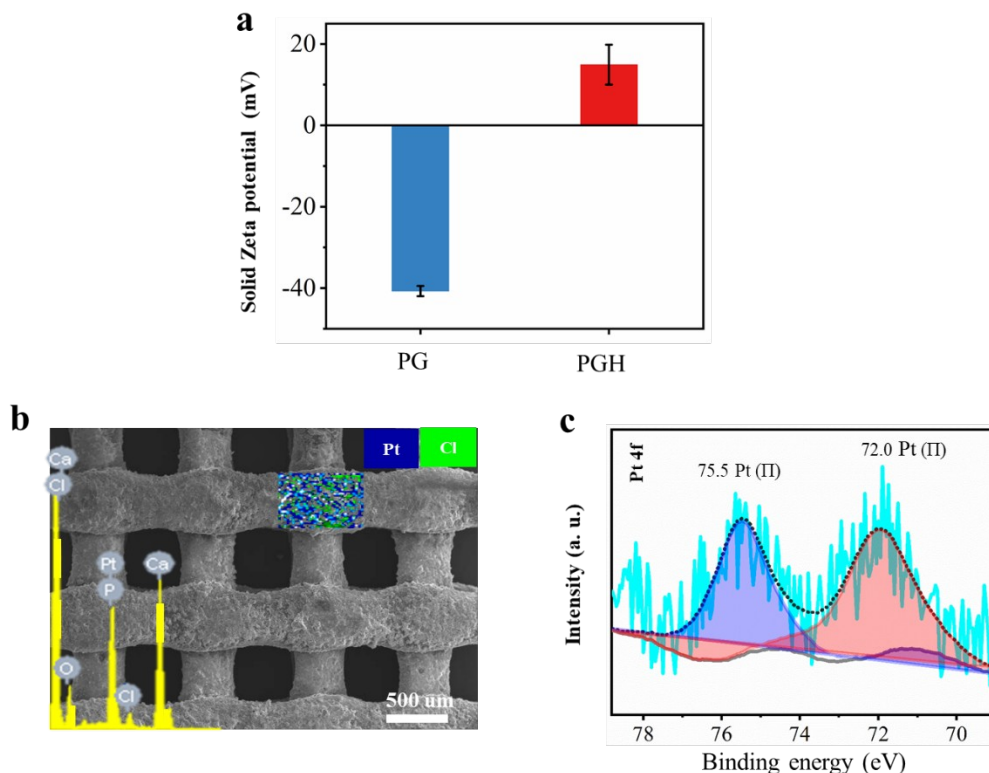
**Fig 3**. The solid Zeta potential of PG (after plasma treatment) and PGH; (**b**) SEM image with inset showing EDS mapping of PGHD; (**c**) XPS spectra showing Pt 4f deconvolution of PGHD.

The temperature profile of PGHD captured in air or in PBS under different laser power density (0.05 $W/cm^2$, 0.15 $W/cm^2$ and 0.30 $W/cm^2$) can be found in **Fig 4a** and **4b**, respectively**.** Results suggest that the phothermal conversion efficiency of the scaffold is dependent on the laser power, irradiation time and the surrounding medium. With laser power > 0.05 $W/cm^2$, the PGHD scaffold can reach > 48 ℃ (therapeutic window for cancer phototherapy) within ~ 40 s under the ambient condition. The curve plateaus after 40 s, indicating stabilization of the temperature with time. When the scaffold was immersed in PBS solution, the laser heating effect was attenuated due to the heat dissipation into the surrounding aqueous medium. With a laser power density of 0.30 $W/cm^2$, the temperature of the scaffold reached 45 ℃ in ~ 100 s. The cumulative release of Pt element was also monitored under conditions with and without NIR irradiation (**Fig 4c**), and the results show that application of NIR irradiation can significantly accelerate the release of DDP.
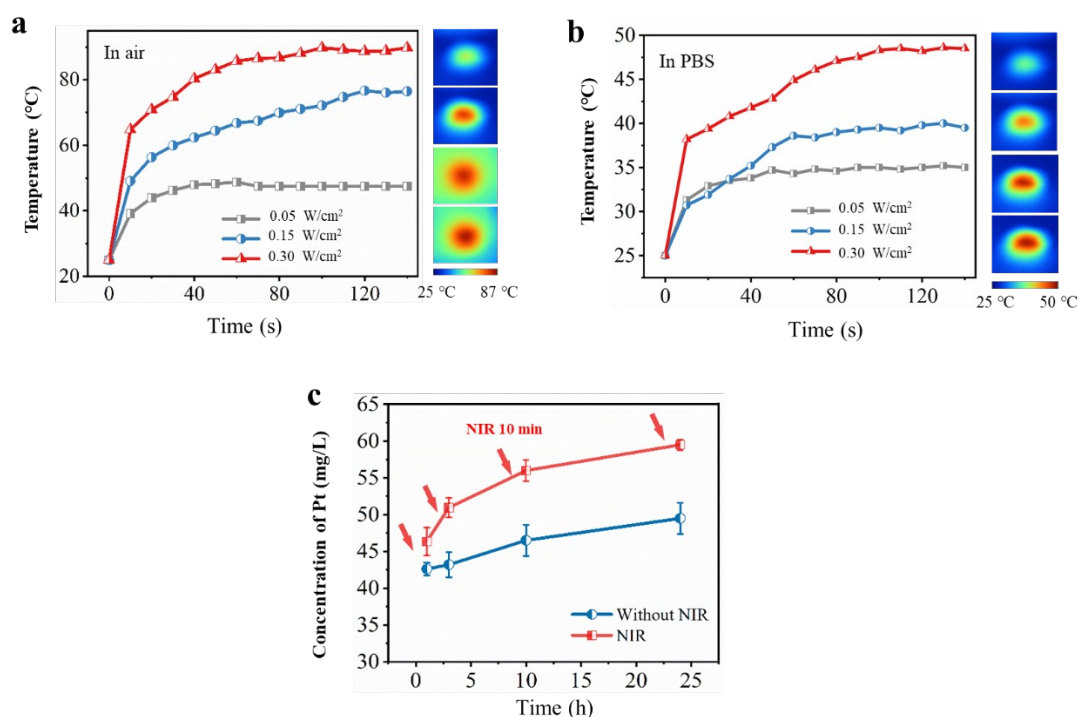
**Fig 4**. Temperature variation of PGHD under NIR irradiation with laser power densities (0.05 W/cm$^2$, 0.15 W/cm$^2$, 0.30 W/cm$^2$) in air (**a**) and in PBS solution (**b**), the inset NIR thermal images (laser power density = 0.30 W/cm$^2$); (**c**) The cumulative release of Pt with and without NIR irradiation, red arrows demote the points where 10 min NIR irradiation was applied.

**Fig 5** shows that the BR of PGH and PGHD against *MRSA* and *E. coli* were about 60 % and 65 %, respectively in the absence of NIR irradiation. One episode of NIR irradiation (0.30 W/cm$^2$, 10 min) can lead to significantly enhanced BR against *MRSA* (99.99%, see **Fig 5a** and **S2**) and *E. coli* (99.99%, see **Fig 5b** and **S3**), indicating the potential of achieving near total eradication of both bacterial strains under combined effect of antibiotics and photothermal conversion.
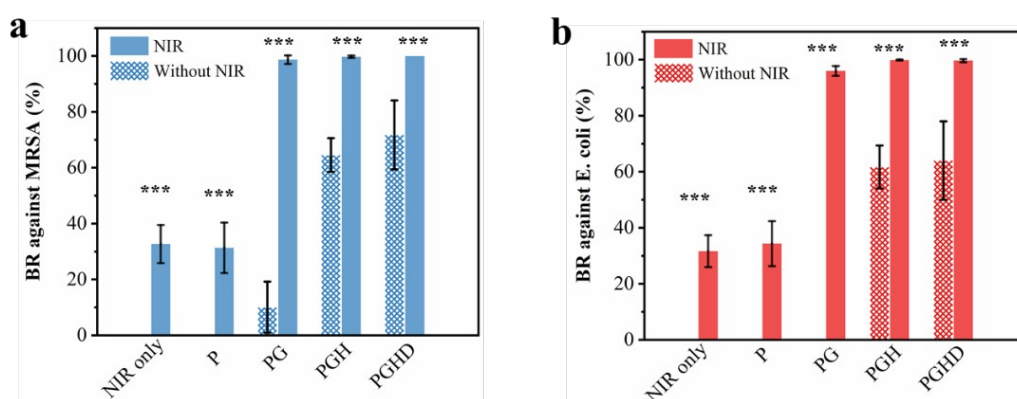
**Fig 5.** Bactericidal rate against *MRSA* (**a**) and *E. coli* (**b**) of P, PG, PGH and PGHD with and without NIR irradiation, ***p < 0.001, **p<0.01, *p<0.05 vs. without NIR.

## Cancer ablation *in vitro*

The CLSM images (**Fig 6a**) showed that without NIR irradiation, MG-63 cells on P, P+, PG, and PGH spread well with strong pseudopodia attachment on the surfaces in all directions. The cells also showed bright cell nuclei and actin in all groups. For PGHD, the presence of cancer drug has led to marked change of MG-63 cell morphology, i.e., round shape with no clear orientation, indicating inhibition of the cell growth. Upon NIR irradiation (0.30 W/cm$^2$ for 10 min), MG-63 cells on all samples displayed round shape with no pseudopodia and featured thinning of the actin layer around the cell nucleus.

The quantitative CCK-8 results of MG-63 (**Fig 6b**) showed that in the absence of NIR irradiation (NIR-), only PGHD demonstrated significantly reduced MG-63 viability (59.8%) due to the presence of anti-cancer drug. All other groups (P, PG, PGH and control) showed no obvious anti-cancer effect (cell viability ~100%). With NIR irradiation, the number of live cells declined drastically in PG+, PGH+ and PGHD+, while the cell viabilities of P, P+, PG, and PGH were similar to that of the control group. Under 0.30 W/cm$^2$ NIR irradiation, the scaffolds (e.g. PG+, PGH+, and PGHD+) could reach the 45 ℃ within 100 s in immersed condition and remain stabilized for the remainder of the treatment time. Literature suggests that the temperature in the range of 45~50 ℃ can result in rapid necrosis of tumor cells (cancer ablation) because of their lower heat tolerance result can result in DNA and protein denaturation [30, 31]. It is worth noting that the cell viability of PGHD+ further decreased to 24.9%, significantly lower than that of PG+ and PGH+ (45.7% and 45.4%, respectively).

The results of live/dead staining **(Fig 6c)** were in accordance with the CCK-8 results., confirming PGHD+ is the most effective group in cancer ablation due to the combined effect of cancer drug release and hyperthermia introduced by PPT.
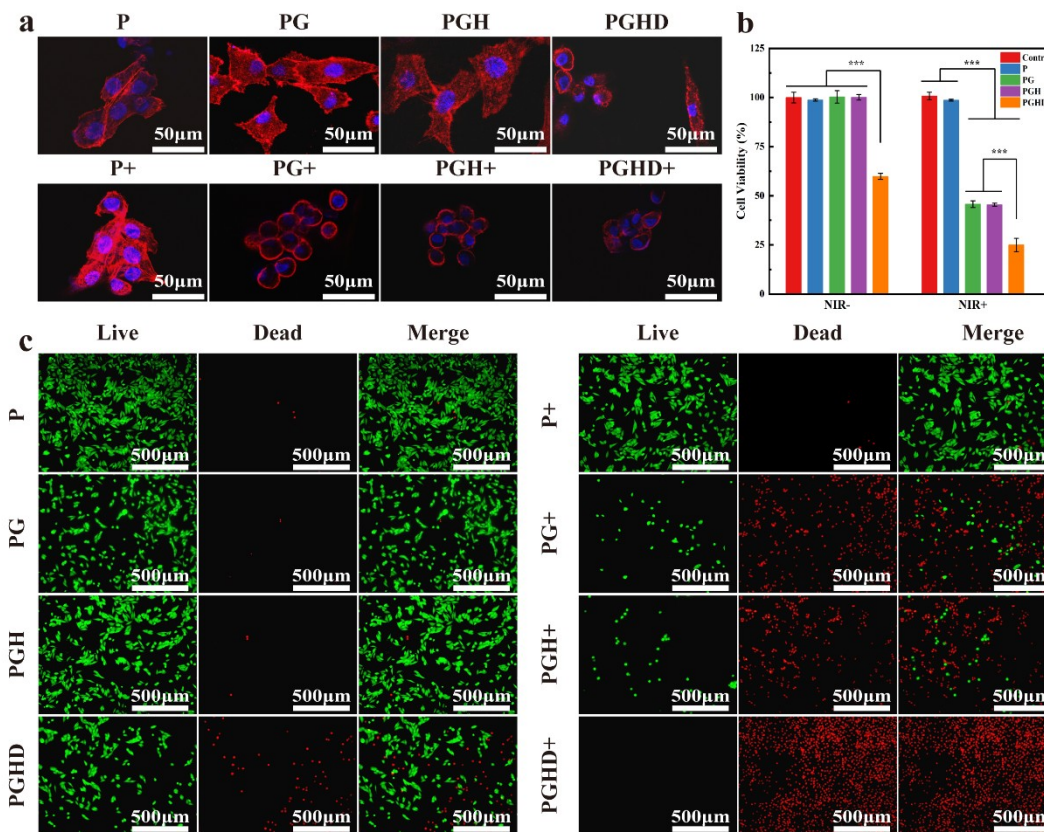
**Fig 6.** *In vitro* **photothermal effect on killing of osteosarcoma cells. (a)** CLSM (red: cytoskeleton; blue: cell nuclei) images of MG-63 in different groups; **(b)** CCK-8 results showed cell viability of MG-63 with and without NIR irradiation; **(c)** Live/dead staining (green: live cells; red: dead cells) images of MG-63 in different groups. (***p < 0.001, **p<0.01, *p<0.05)

**Tumor ablation *in vivo***

Xenograft osteosarcoma model was established in nude mice to evaluate the scaffolds therapeutic effects towards primary bone cancer. When irradiated by NIR (0.30 W/cm$^2$), the tumor tissue containing PG, PGH, and PGHD scaffolds reached > 45 ℃ in 100 s then remain stabilized at ~ 50 ℃ for the remaining treatment time. In contrast, the temperature of P scaffold and the control group remained at ~ 37 ℃ (**Fig 7a** and **7b**). With NIR irradiation (0.30 W/cm$^2$, 10 min/day), the tumor volumes of PG+, PGH+ and PGHD+ showed marked reduction after 10 d, the tumor volume of the PGHD group remain unchanged, and the tumor volumes of the Control, Control+, P, P+, PG, and PGH groups showed significant growth (8~9 times greater than day 0) **(Fig 7c** and **7d)**. Amongst all groups, PGHD+ demonstrated greatest tumor ablation

18

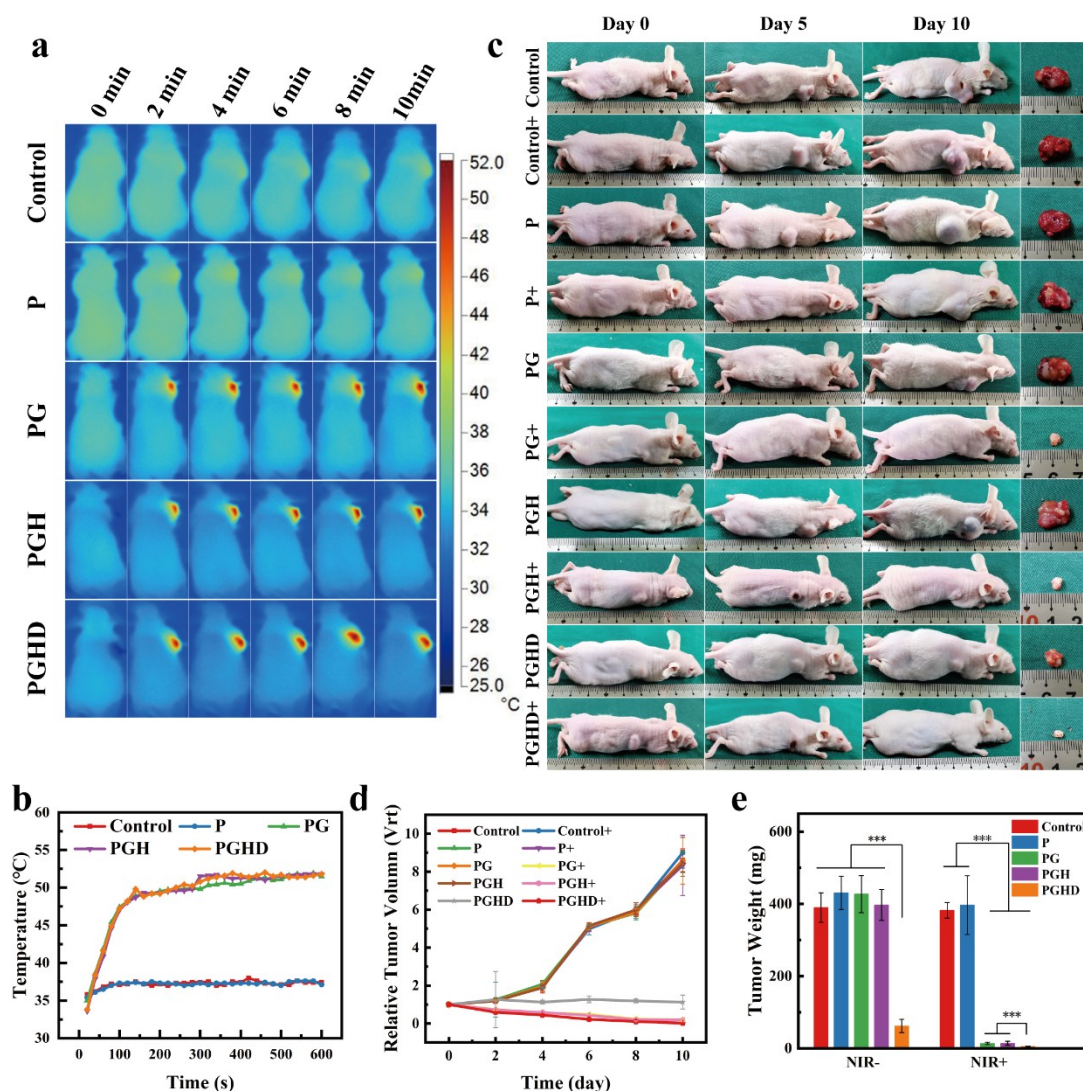efficiency, with 98.5% tumor weight reduction compared to the control **(Fig 7e)**.



**Fig 7.** Infrared thermal images **(a)** and temperature profile **(b)** of tumor tissue recorded during the first episode of laser treatment; **(c)** Representative images of nude mice in different groups on day 0, day 5, and day 10 and tumor tissue obtained from different treatment groups on day 10; **(d)** Relative tumor volume ($V_{rt}$) measured for different groups as a function of time (days); **(e)** Tumor weights measured for different groups on day 10. (***$p < 0.001$, **$p<0.01$, *$p<0.05$)

The reduction of tumor volume and weight can be attributed to the DDP release and/or the photothermal effect of the scaffolds. Without NIR irradiation, the reduction of tumor seen in PGHD is solely due to the presence of DDP. The drug exerted an antiproliferative effect by creating intrastrand and interstrand DNA cross-links, which block the tumor cell DNA replication [32].

With NIR irradiation, significant tumor reduction can be seen for groups

containing photothermal agent G (PG+, PGH+). The laser induced heating can cause irreversible damage to the tumor cells, such as protein dysfunction and ultimately induce cell apoptosis [33]. The greatest tumor volume/weight reduction was demonstrated by PGHD+. The integration of laser heating with cancer drugs for combined chemo-PTT could achieve more potent anticancer effect because of the synergistic effects from the PTT-mediated thermal damage of tumor cells and the enhanced cancer drug release under elevated temperature (see **Fig 4c**). The results of tumor treatment in different groups can be further corroborated by the whole-body bioluminescent images shown in **Fig 8a**. The fluorescent intensity and tumors area in PG+, PGH+ and PGHD+ groups significantly declined on day 10, confirming their favorable anti-tumor effect.

H&E staining images (**Fig 8b**) shows the cancer cell karyorrhexis and karyolysis in different group, the strongest effect was seen for PGHD+, followed by PG+ and PGH+, then PGHD. Tumor cell necrosis was not evident in other groups.

The body weight of the mice from all groups had no significant change during the 10 days observation period (**Fig S**). H&E staining images in **Fig 8c** suggest no abnormality was found in heart, liver, spleen, lungs, and kidney in all groups, indicating the minimum side effects of the treatment protocol.
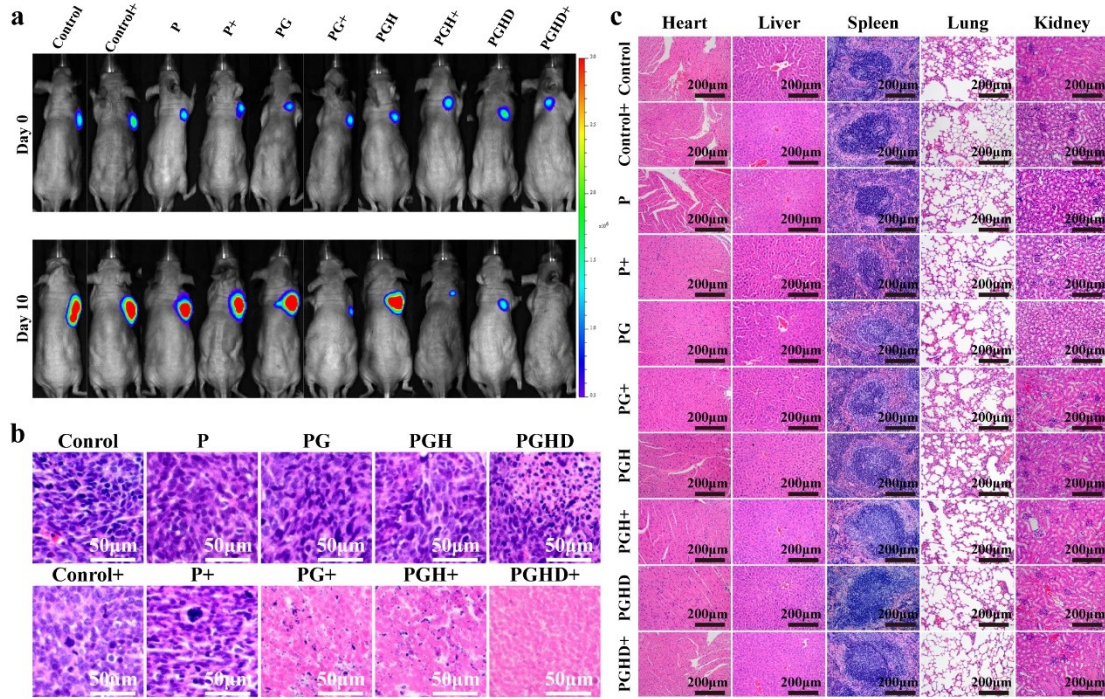
**Fig 8.** (**a**) The whole-body fluorescence imaging of tumor in ten groups at day 0 and day 10; (**b**) H&E staining images of UMR-106-LUC tumor tissue implanted with different scaffolds with and without NIR irradiation; (**c**) H&E staining of selected organs (hearts, livers, spleens, lungs, and kidneys) to evaluate the potential side effects of the therapy.

## Cytocompatibility assessment *in vitro*

MC3T3-E1 cell morphologies on different scaffolds were investigated by CLSM after 24 h incubation (**Fig 9a**). For all groups (P, PG, PGH, and PGHD), the adherent cells fully spread showing evident filopodia structures and extended mature F-actin intracellular stress fibers. Live/dead staining images after 24 h incubation (**Fig 9b**) revealed that the MC3T3-E1 cells grew well on all samples with minimum cell death, indicating the excellent cytocompatibility of all testing groups. The CCK-8 result showed that all scaffolds promoted cell growth over time (**Fig 9c**). All groups showed comparable cell proliferation on day 1, which steadily increased over time. The MC3T3-E1 cells showed a greater proliferation in PGH and PGHD, followed by PG and P (P > 0.05), indicating the presence of HA promoted cell proliferation.
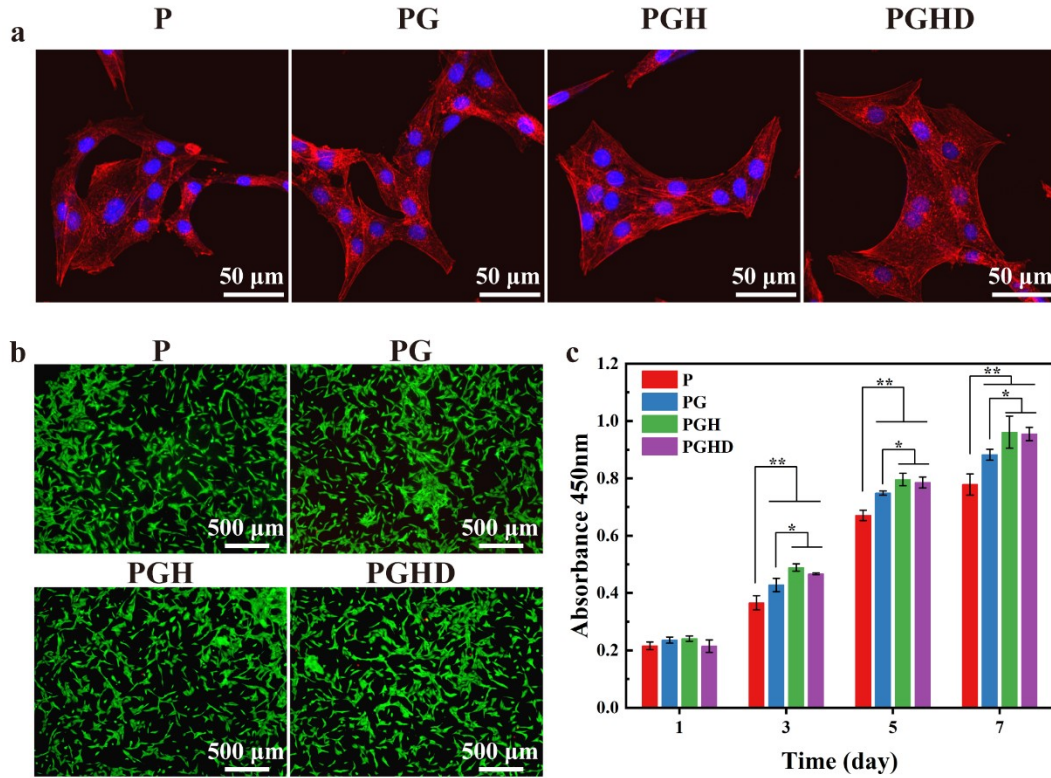
**Fig 9. (a)** CLSM images of MC3T3-E1 cells after culturing with different scaffolds for 1 day; **(b)** Live/dead staining (green: live cells; red: dead cells) images of MC3T3-E1 cells in different groups; **(c)** CCK-8 of MC3T3-E1 cells cultured with different scaffolds for day 1, 3, 5 and 7 respectively. (***$p < 0.001$, **$p<0.01$, *$p<0.05$).

## *In vitro* and *in vivo* osteogenic differentiation

The bone regeneration is essential for bone defect repair. Osteogenic differentiation of the scaffolds was investigated both *in vitro* and *in vivo* and related markers were quantified by real-time PCR (**Fig 10a**). ALP, OPN and OCN are the corresponding makers representing different stages of osteogenic differentiation (ALP: early stage; OPN: secondary stage; OCN: late stage.) [34, 35]. Col-I is one of the key components of extra cellular matrix deposition [36]. After culturing for 7 days, the gene expressions of ALP, OPN, OCN and Col1α1 in PG, PGH and PGHD were significantly upregulated as compared to P, where PGH and PGHD had similar performance. The osteo-related protein expressions of different scaffolds were also evaluated by immunofluorescence (**Fig 10b** and **10c**). The highest OPN and OCN fluorescence intensity was observed in PGH and PGHD, followed by PG and then P. The trend was consistent with what was observed from the real-time PCR results.
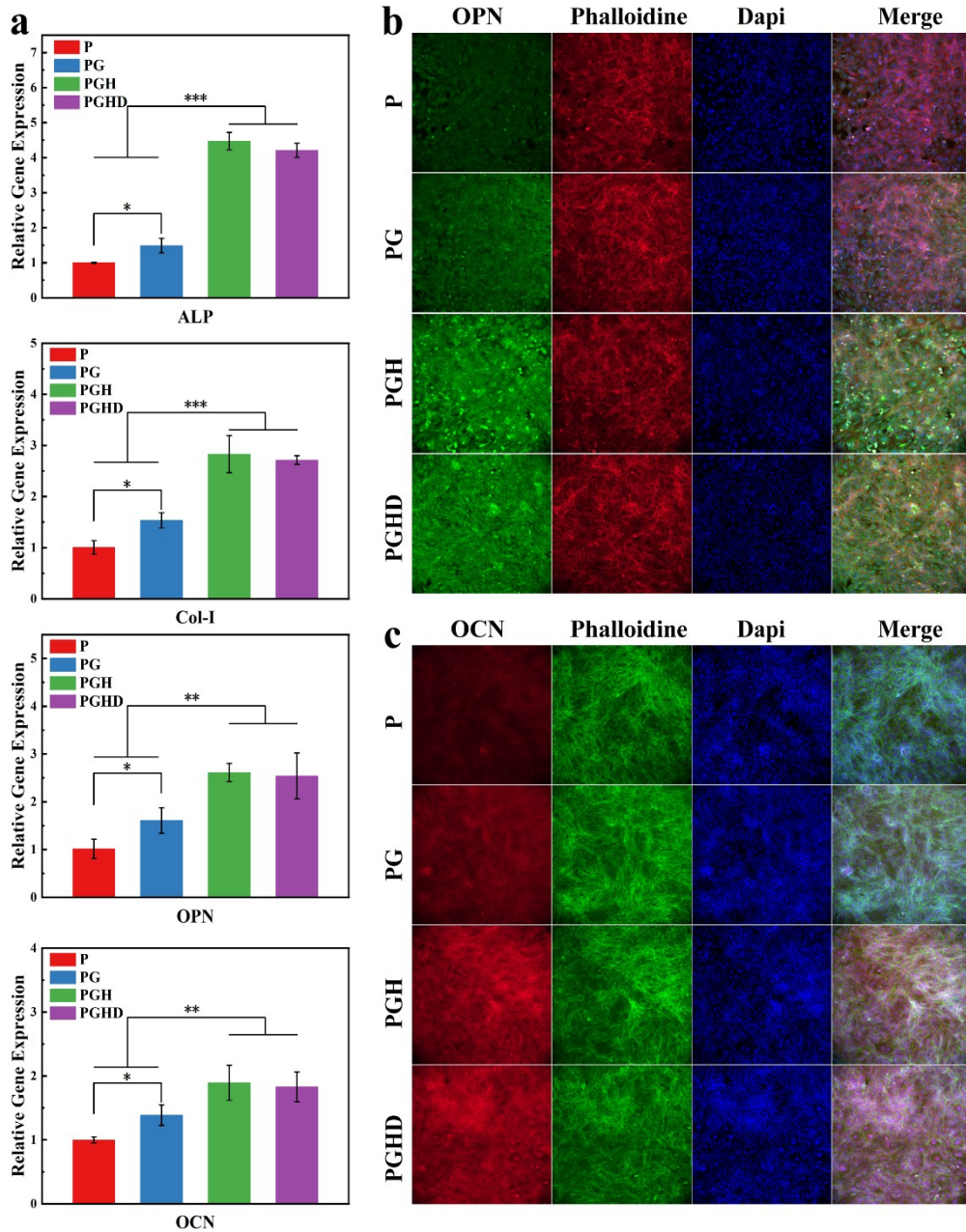
**Fig 10.** (**a**) Real-time PCR analysis results of osteogenic genes (ALP, Col-I, OPN, and OCN) in different groups; (**b, c**) Representative immunofluorescent images of OPN and OCN in different groups. (***p < 0.001, **p<0.01, *p<0.05).

**Fig 11** showed the quantitative and qualitative ALP expressions of MC3T3-E1 pre-osteoblasts in different groups. The ALP-positive areas were the greatest in PGH and PGHD groups, followed by PG and P group, see **Fig 11a**. Quantitative ALP analysis in **Fig 11b** further confirmed this trend. Alizarin red staining was used to detect the osteogenic differentiation, see **Fig 11c** and **11d**. Results show that more

calcium nodules (stained red) were present in PGH and PGHD groups than in PG and P groups.
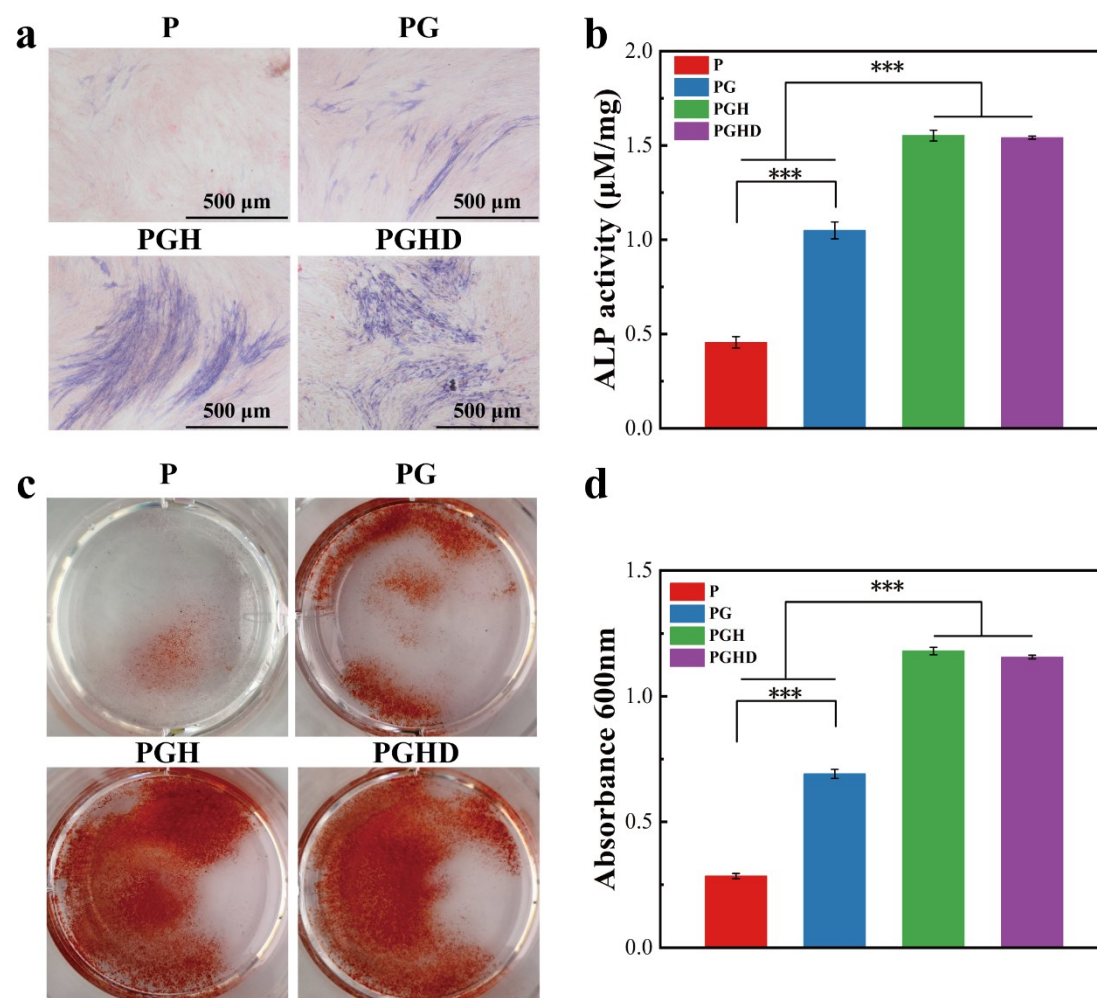


**Fig 11. (a)** Representative ALP staining images and **(b)** quantitative analysis of ALP activity on day 7 in different groups; Alizarin Red S staining **(c)** and quantitative analysis **(d)** of calcium nodules on day 21. (***p < 0.001, **p<0.01, *p<0.05).

The above *in vitro* osteogenic differentiation data revealed that the bone-regeneration capability of different groups follows the order: PGH and PGHD>PG>P. The best osteogenesis ability demonstrated by PGH and PGHD groups can be attributed to the presence of nanostructured HA coating, which promoted the serum protein adsorption, cell adhesion, attachment and and proliferation [37]. The calcium and phosphate ions released from HA can also upregulate the expression of osteogenic genes and activate secretion and extracellular matrix mineralization [38]. The

presence of G in PEEK of PG group also demonstrated improved the scaffold osteogenic differentiation due to the osteoinductive capability of G [39, 40].

The rat femoral specimens (distal femoral condyle) harvested 8 weeks post-surgery are shown in **Fig 12a**. Micro-CT images in **Fig 12b** provide strong evidence of new bone formation and ingrowth towards the center of the bone defect over time. The bone defects in PGH and PGHD groups showed faster healing as compared to PG and P groups. Quantitative analysis showed that BV/TV and Tb. N were significantly greater (while Tb. Sp was significantly lower) in PGH and PGHD groups than those in P and PG groups **(Fig 12c)**. The histological staining images in **Fig 12d** further corroborate these results. That is, larger area of new bone tissues was observed within the scaffolds in PGH and PGHD groups. Sequential fluorescent labeling was used to record and monitor new bone formation around the scaffolds by applying AL and CA **(Fig 12e)**. The fluorescent bands were thick and dense in PGH and PGHD groups but were thin and sparse in P and PG groups, indicating the PGH and PGHD scaffolds promote osteogenesis better. Quantitative analysis of the stained area (**Fig 12f**) shows

that the area% of AL and CA stained bone follows: PGH and PGHD $>$ PG $>$ P, indicating that PGH and PGHD scaffolds have better bone regeneration effects at each point of observation.
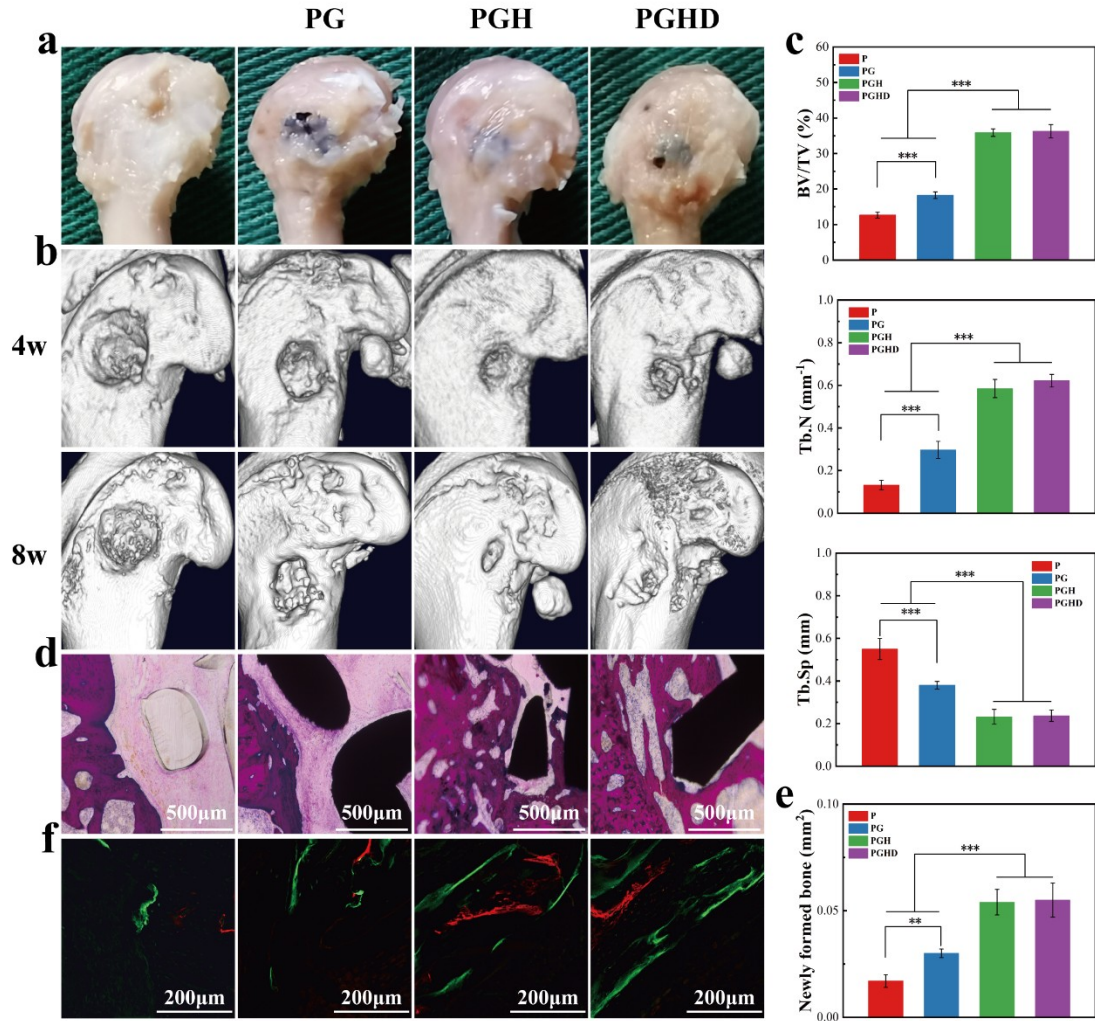
**Fig 12.** (**a**) Representative images of femurs implanted with different scaffolds; (**b**) Representative three-dimensional reconstructed micro-CT images at week 4 and week 8 after surgery; (**c**) Quantitative analysis of newly formed bone tissues depend on three-dimensional reconstructed micro-CT (BV/TV, Tb. N, and Tb. Sp) at week 8 postoperatively; (**d**) Representative images of histological staining (fuchsine-methylene blue) in different groups at 8 weeks postoperatively; (**e**) Quantitative analysis of newly formed bone tissue depends on pathological sections; **(f)** Sequential fluorescent labeling observation. Red and green represent labeling by AL (week 3) and CA (week 6), respectively (***p < 0.001, **p<0.01, *p<0.05).

Clinical translation of biomedical materials/products replies on rigorous *in vitro* and *in vivo* studies. Well-designed correlation analysis may help to identify the key *in vitro* parameters that can be used to predict the bone regeneration capacity *in vivo*. This could subsequently reduce the economic and time-cost for *in vivo* studies [41]. In this study, Pearson's correlation test was used to analyze the relationship between the biocompatibility parameters (CCK8-1d, 3d, 5d and 7d), osteogenesis-related genes

(ALP, Col-I, OCN, and OPN), and *in vivo* bone regeneration parameters (BV/TV, Tb. N, and Tb. sp). The correlation test data in **Fig 13** suggests that certain parameters under the same category (i.e., CCK8-3d and CCK8-5d; ALP, Col-I, and OCN; Tb. N, and Tb. sp) have strong correlation with each other. Furthermore, Col-I and OCN have strong correlation with Tb. N and Tb. sp. The results suggest that osteogenesis-related genes identified in our *in vitro* studies can serve as an important index for predicting the implants bone regeneration capacity *in vivo*.
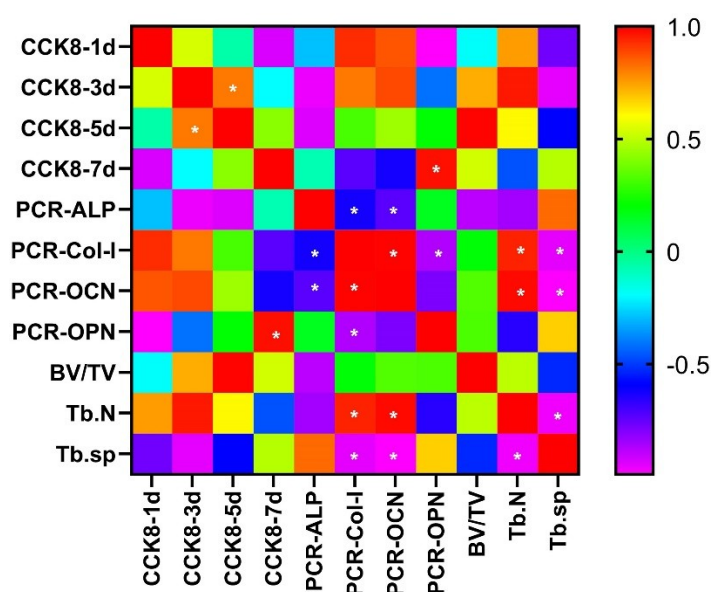


**Fig 13.** Confusion matrix (heatmap) of *in vitro* and *in vivo* parameters concerning bone formation according to Pearson's correlation test. The color intensity indicates the magnitude of the correlation coefficient, ranging from −1 to 1. (***p < 0.001, **p<0.01, *p<0.05).

## Conclusion

In this study, we design and developed a 3D printed hybrid PEEK/graphene scaffolds with drug laden bioactive hydroxyl apatite coating. The scaffold has tailored porous structure / mechanical properties, and has combined drug release/photothermal therapeutic function. Results show that the scaffold with loaded antibiotic and/or anti-cancer drugs and on-demand photothermal conversion effect can achieve near total eradication of *Escherichia coli* (*E. coli*) and *Methicillin-resistant Staphylococcus*

*aureus* (MR*SA*), as well as effective ablation of osteosarcoma cancer cells. The coated scaffold also exhibited strong bone regeneration ability, demonstrating its strong potential in applications such as bone defect repair as well as multimodal management of osteosarcoma and osteomyelitis.

## Acknowledgements

## References

1. Moore, D.D. and H.H. Luu, *Osteosarcoma.* Cancer Treat Res, 2014. **162**: p. 65-92.

2. Anderson, M.E., *Update on Survival in Osteosarcoma.* Orthop Clin North Am, 2016. **47**(1): p. 283-292.

3. Zhang, Y., et al., *Tumor targeted combination therapy mediated by functional macrophages under fluorescence imaging guidance.* Journal of Controlled Release, 2020. **328**: p. 127-140.

4. Wang, Y., et al., *Highly Penetrable and On-Demand Oxygen Release with Tumor Activity Composite Nanosystem for Photothermal/Photodynamic Synergetic Therapy.* ACS Nano, 2020. **14**(12): p. 17046-17062.

5. Shi, C., et al., *Catalase-based liposomal for reversing immunosuppressive tumor microenvironment and enhanced cancer chemo-photodynamic therapy.* Biomaterials, 2020. **233**: p. 119755.

6. Nam, J., et al., *Chemo-photothermal therapy combination elicits anti-tumor immunity against advanced metastatic cancer.* Nature Communications, 2018. **9**(1): p. 1074.

7. He, M., et al., *Conducting Polyetheretherketone Nanocomposites with an Electrophoretically Deposited Bioactive Coating for Bone Tissue Regeneration and Multimodal Therapeutic Applications.* ACS Appl Mater Interfaces, 2020. **12**(51): p. 56924-56934.

8.    Dang, W., et al., *A bifunctional scaffold with CuFeSe₂ nanocrystals for tumor therapy and bone reconstruction.* Biomaterials, 2018. **160**: p. 92-106.

9.    Ma, H., et al., *3D printing of high-strength bioscaffolds for the synergistic treatment of bone cancer.* NPG Asia Materials, 2018. **10**(4): p. 31-44.

10.   Ma, H., et al., *A Bifunctional Biomaterial with Photothermal Effect for Tumor Therapy and Bone Regeneration.* Advanced Functional Materials, 2016. **26**(8): p. 1197-1208.

11.   GhavamiNejad, A., et al., *pH/NIR Light-Controlled Multidrug Release via a Mussel-Inspired Nanocomposite Hydrogel for Chemo-Photothermal Cancer Therapy.* Scientific Reports, 2016. **6**(1): p. 33594.

12.   Yang, F., et al., *Magnetic Mesoporous Calcium Sillicate/Chitosan Porous Scaffolds for Enhanced Bone Regeneration and Photothermal-Chemotherapy of Osteosarcoma.* Scientific Reports, 2018. **8**(1): p. 7345.

13.   Gao, C., et al., *Advances in biocermets for bone implant applications.* Bio-Design and Manufacturing, 2020. **3**(4): p. 307-330.

14.   Zhu, Y., et al., *Bone regeneration with micro/nano hybrid-structured biphasic calcium phosphate bioceramics at segmental bone defect and the induced immunoregulation of MSCs.* Biomaterials, 2017. **147**: p. 133-144.

15.   Nieminen, T., et al., *Amorphous and crystalline polyetheretherketone: Mechanical properties and tissue reactions during a 3-year follow-up.* J Biomed Mater Res A, 2008. **84**(2): p. 377-383.

16.   Yuan, B., et al., *Comparison of osteointegration property between PEKK and PEEK: Effects of surface structure and chemistry.* Biomaterials, 2018. **170**: p. 116-126.

17.   Grupp, T.M., et al., *Biotribology of a new bearing material combination in a rotating hinge knee articulation.* Acta Biomaterialia, 2013. **9**(6): p. 7054-7063.

18.   Zhu, C., et al., *Titanium-interlayer mediated hydroxyapatite coating on polyetheretherketone: a prospective study in patients with single-level cervical degenerative disc disease.* Journal of Translational Medicine, 2021. **19**(1): p. 14.

19.   Dodier, P., et al., *Single-stage bone resection and cranioplastic reconstruction: comparison of a novel software-derived PEEK workflow with the standard reconstructive method.* International Journal of Oral and Maxillofacial Surgery, 2020. **49**(8): p. 1007-1015.

20.   Di Maggio, B., et al., *PEEK radiolucent plate for distal radius fractures: multicentre clinical results at 12 months follow up.* Injury, 2017. **48**: p. S34-S38.

21.   Berretta, S., K. Evans, and O. Ghita, *Additive manufacture of PEEK cranial implants: Manufacturing considerations versus accuracy and mechanical performance.* Materials & Design, 2018. **139**: p. 141-152.

22.   He, M., et al., *Super tough graphene oxide reinforced polyetheretherketone for potential hard tissue repair applications.* Composites Science and Technology, 2019. **174**: p. 194-201.

23.   Zhu, S., et al., *Graphene Reinforced Polyether Ether Ketone Nanocomposites for Bone Repair Applications.* ChemRixv Preprint, 2020: p. https://doi.org/10.26434/chemrxiv.13289525.v1.

24.   *Modification of polyetheretherketone (PEEK) implants: from enhancing bone integration to enabling multi-modal therapeutics - A review of the state-of-the-art and future outlook.* 10.2139/ssrn.3797424.

25.   Zhou, S., et al., *Effects of Ethylene-Vinyl Acetate Copolymer on the Morphology and Mechanical Properties of Hydroxyapatite/Polyamide 66 Composites for Bone Tissue Engineering.*

Polymer-Plastics Technology and Engineering, 2014. **53**(3): p. 290-297.

26.    Wei, J. and Y. Li, *Tissue engineering scaffold material of nano-apatite crystals and polyamide composite.* European Polymer Journal, 2004. **40**(3): p. 509-515.

27.    Sun, M., et al., *Effective treatment of drug-resistant lung cancer via a nanogel capable of reactivating cisplatin and enhancing early apoptosis.* Biomaterials, 2020. **257**: p. 120252.

28.    Zhu, J., et al., *Polymeric antimicrobial membranes enabled by nanomaterials for water treatment.* Journal of Membrane Science., 2018. **550**: p. 173-197.

29.    Shi, L., et al., *The Improved Biological Performance of a Novel Low Elastic Modulus Implant.* PLOS ONE, 2013. **8**(2): p. e55015.

30.    Liu, Y., et al., *3D-printed scaffolds with bioactive elements-induced photothermal effect for bone tumor therapy.* Acta Biomater, 2018. **73**: p. 531-546.

31.    Luo, S., et al., *An Injectable, Bifunctional Hydrogel with Photothermal Effects for Tumor Therapy and Bone Regeneration.* Macromol Biosci, 2019. **19**(9): p. e1900047.

32.    Wagner, J.M. and L.M. Karnitz, *Cisplatin-Induced DNA Damage Activates Replication Checkpoint Signaling Components that Differentially Affect Tumor Cell Survival.* Molecular Pharmacology, 2009. **76**(1): p. 208.

33.    Shi, M., et al., *A Protein-Binding Molecular Photothermal Agent for Tumor Ablation.* Angew Chem Int Ed Engl, 2021.

34.    Li, G., et al., *Enhanced Osseointegration of Hierarchical Micro/Nanotopographic Titanium Fabricated by Microarc Oxidation and Electrochemical Treatment.* ACS Appl Mater Interfaces, 2016. **8**(6): p. 3840-52.

35.    Xu, X., et al., *Triple-functional polyetheretherketone surface with enhanced bacteriostasis and anti-inflammatory and osseointegrative properties for implant application.* Biomaterials, 2019. **212**: p. 98-114.

36.    Cheng, M., et al., *Calcium Plasma Implanted Titanium Surface with Hierarchical Microstructure for Improving the Bone Formation.* ACS Appl Mater Interfaces, 2015. **7**(23): p. 13053-61.

37.    Lu, M., et al., *The morphological effect of nanostructured hydroxyapatite coatings on the osteoinduction and osteogenic capacity of porous titanium.* Nanoscale, 2020. **12**(47): p. 24085-24099.

38.    Ali Akbari Ghavimi, S., et al., *Calcium and phosphate ions as simple signaling molecules with versatile osteoinductivity.* Biomedical Materials, 2018. **13**(5): p. 055005.

39.    Shadjou, N., M. Hasanzadeh, and B. Khalilzadeh, *Graphene based scaffolds on bone tissue engineering.* Bioengineered, 2018. **9**(1): p. 38-47.

40.    Elkhenany, H., et al., *Graphene supports in vitro proliferation and osteogenic differentiation of goat adult mesenchymal stem cells: potential for bone tissue engineering.* J Appl Toxicol, 2015. **35**(4): p. 367-74.

41.    Yuan, B., et al., *A biomimetically hierarchical polyetherketoneketone scaffold for osteoporotic bone repair.* Sci Adv, 2020. **6**(50).